



ALMA Detection of a Linearly Polarized Reverse Shock in GRB 190114C

Tanmoy Laskar¹, Kate D. Alexander^{2,8}, Ramandeep Gill³, Jonathan Granot³, Edo Berger⁴, C. G. Mundell¹, Rodolfo Barniol Duran⁵, J. Bolmer⁶, Paul Duffell⁴, Hendrik van Eerten¹, Wen-fai Fong², Shiho Kobayashi⁷, Raffaella Margutti², and Patricia Schady¹

¹ Department of Physics, University of Bath, Claverton Down, Bath BA2 7AY, UK

² Center for Interdisciplinary Exploration and Research in Astrophysics (CIERA) and Department of Physics and Astronomy, Northwestern University, Evanston, IL 60208, USA

³ Department of Natural Sciences, The Open University of Israel, PO Box 808, Ra'anana 43537, Israel

⁴ Center for Astrophysics, Harvard & Smithsonian, 60 Garden Street, Cambridge, MA 02138, USA

⁵ Department of Physics and Astronomy, California State University, Sacramento, 6000 J Street, Sacramento, CA 95819, USA

⁶ Max-Planck-Institut für extraterrestrische Physik, Giessenbachstraße, D-85748 Garching, Germany

⁷ Astrophysics Research Institute, Liverpool John Moores University, IC2, Liverpool Science Park, 146 Brownlow Hill, Liverpool L3 5RF, UK

Received 2019 April 15; revised 2019 May 10; accepted 2019 May 17; published 2019 June 13

Abstract

We present Atacama Large Millimeter/submillimeter Array 97.5 GHz total intensity and linear polarization observations of the mm-band afterglow of GRB 190114C spanning 2.2–5.2 hr after the burst. We detect linear polarization at the $\approx 5\sigma$ level, decreasing from $\Pi = (0.87 \pm 0.13)\%$ to $(0.60 \pm 0.19)\%$, and evolving in polarization position angle from $(10 \pm 5)^\circ$ to $(-44 \pm 12)^\circ$ during the course of the observations. This represents the first detection and measurement of the temporal evolution of polarized radio/millimeter emission in a γ -ray burst. We show that the optical and X-ray observations between 0.03 days and ~ 0.3 days are consistent with a fast-cooling forward shock expanding into a wind environment. However, the optical observations at $\lesssim 0.03$ days, as well as the radio and millimeter observations, arise from a separate component, which we interpret as emission from the reverse-shocked ejecta. Using the measured linear polarization, we constrain the coherence scale of tangled magnetic fields in the ejecta to an angular size of $\theta_B \approx 10^{-3}$ radian, while the rotation of the polarization angle rules out the presence of large-scale, ordered axisymmetric magnetic fields, and in particular a large-scale toroidal field, in the jet.

Key words: gamma-ray burst: general – gamma-ray burst: individual (GRB 190114C) – polarization

1. Introduction

The interaction of gamma-ray burst (GRB) jets with their ambient medium generates two shocks: (i) a relativistic forward shock (FS) in the ambient medium that powers the long-lasting X-ray to radio afterglow radiation, and (ii) a short-lived reverse shock (RS) propagating into, and decelerating, the jet (Sari et al. 1998; Zhang & Kobayashi 2005). Whereas observations and modeling of the FS emission reveal the burst energetics, outflow geometry, and the density structure of the pre-explosion environment, the self-similar hydrodynamic evolution of the FS is insensitive to the composition of the jet itself.

Instead, the composition (baryon content), initial Lorentz factor, and magnetization of GRB jets can be probed through the short-lived RS emission (Granot & Königl 2003; Granot & Taylor 2005; Zhang & Kobayashi 2005). The expected signature of RS synchrotron radiation is a bright optical flash as the shock crosses the ejecta (typically lasting a few tens of seconds) followed by a radio flare (typically lasting a few days), a phenomenon predicted to be prevalent, if not ubiquitous, in GRBs (Akerlof et al. 1999; Sari & Piran 1999). Isolating the RS requires careful decomposition of the observed multi-frequency (radio-to-X-ray) spectral energy distribution (SED) at different epochs into FS and RS contributions (Laskar et al. 2013; Perley et al. 2014; van der Horst et al. 2014; Laskar et al. 2016; Alexander et al. 2017; Laskar et al. 2018a, 2018b).

RS emission is expected to be polarized, particularly if the jet contains large-scale ordered magnetic fields advected from

the central engine (Granot & Königl 2003; Granot & Taylor 2005), and thus RS polarization observations provide a powerful measure of ejecta magnetization (Mundell et al. 2013). The degree of RS polarization is sensitive to the magnetic field anisotropy in the jet, with levels of up to $\approx 60\%$ expected in the presence of ordered magnetic fields or $\lesssim 10\%$ in the case of tangled fields (Granot 2003; Granot & Königl 2003; Lyutikov et al. 2003). The polarization angle is predicted to remain stable in jets with large-scale magnetic fields (Lazzati et al. 2004), or vary randomly with time if the field is produced locally by plasma or magnetohydrodynamic (MHD) instabilities (Gruzinov & Waxman 1999). Thus measurements of polarization degree and position angle, and of the evolution of these quantities with time, should provide diagnostics for the magnetic field structure in GRB jets.

Polarized RS emission in the radio or millimeter band has not been detected to date due to sensitivity and response time limitations, with the best limits of $\lesssim 7\%$ (linear) and $\lesssim 9\%$ (circular) for likely RS emission in GRB 991216 at 8.46 GHz, 1.5 days after the burst (Granot & Taylor 2005), and $< 3.9\%$ (linear) and $< 2.7\%$ (circular) at 1.5 days after the burst for the strong RS observed in GRB 130427A (van der Horst et al. 2014). However, RS emission, although visible for up to \sim a week in the cm-band, is often self-absorbed at these frequencies (Laskar et al. 2013, 2016, 2018a, 2018b); as self-absorption suppresses intrinsic polarization (Toma et al. 2008), this could potentially explain the cm-band upper limits. In contrast, RS emission is expected to be optically thin in the mm-band; however, the limited sensitivity and response time of mm-band facilities has precluded such a measurement to date.

⁸ Einstein Fellow.

Here, we present Atacama Large Millimeter/submillimeter Array (ALMA) Band 3 (97.5 GHz) full Stokes observations of GRB 190114C, beginning at 2.2 hr after the burst and lasting for 3 hr, together with the Karl G. Jansky Very Large Array (VLA) observations spanning 4.7–6.3 hr after the burst. Our data reveal the first polarization detection⁹ at radio or millimeter frequencies. By combining the radio, millimeter, optical, and X-ray observations, we demonstrate that the mm-band flux is dominated by an RS, which allows us to constrain the magnetic field geometry in the outflow powering this burst. We assume $\Omega_m = 0.31$, $\Omega_\lambda = 0.69$, and $H_0 = 68 \text{ km s}^{-1} \text{ Mpc}^{-1}$. All times are relative to the *Swift* trigger time and in the observer frame, unless otherwise indicated.

2. GRB Properties and Observations

2.1. Gamma-Ray, X-Ray, and Optical

GRB 190114C was discovered by the Burst Alert Telescope (BAT; Barthelmy et al. 2005) on the *Neil Gehrels Swift Observatory* (*Swift*; Gehrels et al. 2004) on 2019 January 14 at 20:57:03 UT (Gropp et al. 2019). The GRB was also detected by *Konus-Wind* in the 30 keV to 20 MeV band, which observed decaying emission until ≈ 320 s after the trigger (Frederiks et al. 2019), by the *Fermi* Gamma-ray Burst Monitor (GBM; Meegan et al. 2009) with $T_{90} \approx 116$ s, and by the *Fermi* Large Area Telescope (Hamburg et al. 2019; Kocevski et al. 2019). In a historic first, high-energy emission from this burst was also detected by the twin Major Atmospheric Gamma Imaging Cherenkov (MAGIC) telescopes at $\gtrsim 300$ GeV, starting 50 s after the BAT trigger (Mirzoyan et al. 2019).

The optical afterglow was discovered by the *Swift* UV/Optical Telescope (UVOT; Roming et al. 2005) starting 73 s after the BAT trigger (Gropp et al. 2019). Spectroscopic observations with the ALFOSC instrument on the Nordic Optical Telescope (NOT) beginning ≈ 29 minutes after the BAT trigger yielded a redshift of $z = 0.42$ (Selsing et al. 2019), which was further refined with X-shooter spectroscopy at the European Southern Observatory’s Very Large Telescope to $z = 0.4245$ (Kann et al. 2019).

The *Swift* X-ray Telescope (XRT; Burrows et al. 2005) began observing GRB 190114C 64 s after the BAT trigger. We use the photon index for WT- and PC-mode observations listed on the *Swift* website, together with the corresponding unabsorbed counts-to-flux conversion rate to convert the 0.3–10 keV count rate light curve¹⁰ to flux density at 1 keV. We performed photometry on the UVOT data at 6×10^{-3} days with a $3''.5$ aperture (including aperture corrections) using standard techniques (Poole et al. 2008). We further include observations of the afterglow reported in GCN circulars, in particular, the NOT observations at 2×10^{-2} days (Selsing et al. 2019) and the GROND observations at ≈ 0.16 days (Bolmer & Schady 2019).

2.2. Radio: VLA

We observed the afterglow using the VLA starting 4.7 hr (≈ 0.2 days) after the burst through program 18A-088 (PI: T. Laskar). In our first epoch, we obtained a full sequence of

⁹ We note that a manuscript reporting detection of polarized mm-band emission in GRB 171205A at ≈ 5.2 days after the burst appeared at <https://arxiv.org/abs/1904.08111> two days after our article was posted on arXiv.

¹⁰ Obtained from the *Swift* website at http://www.swift.ac.uk/xrt_curves/883832 and re-binned to a minimum signal-to-noise ratio per bin of 10.

Table 1
Radio and Millimeter Stokes *I* Observations of GRB 190114C

Telescope	Frequency (GHz)	Time (days)	Flux Density (mJy)	Uncertainty (μ Jy)
ALMA	97.5	0.0995	11.5	21.8
ALMA	97.5	0.107	11.1	21.2
ALMA	97.5	0.115	10.7	25.7
ALMA	97.5	0.125	10.2	31.4
ALMA	97.5	0.129	10.1	60.8
ALMA	97.5	0.140	9.58	20.8
ALMA	97.5	0.146	9.26	35.5
ALMA	97.5	0.154	8.60	29.6
ALMA	97.5	0.161	8.24	22.2
ALMA	97.5	0.168	8.05	25.5
ALMA	97.5	0.188	7.53	23.0
ALMA	97.5	0.196	7.27	23.1
ALMA	97.5	0.203	7.04	23.7
ALMA	97.5	0.213	7.00	28.8
ALMA	97.5	0.217	6.87	56.7
VLA	37.0	0.197	3.95	39.0
VLA	30.0	0.197	3.28	32.0
VLA	24.5	0.219	2.66	23.0
VLA	19.2	0.219	1.96	18.0
VLA	16.0	0.236	1.52	24.4
VLA	13.5	0.236	1.22	29.9
VLA	11.0	0.249	0.838	19.0
VLA	8.55	0.249	0.607	17.3
VLA	7.10	0.261	0.397	19.3
VLA	5.00	0.261	0.118	32.0

observations spanning 5–38 GHz. We used 3C48 as the flux density and bandpass calibrator and J0402-3147 as the complex gain calibrator. We carried out data reduction with CASA (McMullin et al. 2007) using the `pwkit` package (Williams et al. 2017). The highest-frequency (*K*- and *Ka*-band) observations exhibited significant post-calibration residuals, which we remedied using phase-only self-calibration. We are continuing observations of the afterglow in the cm-band at the time of writing, and defer a detailed analysis of the cm-band properties of this event at $\gtrsim 1$ day to a future work. We list the results of our VLA observations in Table 1.

2.3. ALMA Polarization Observations

We obtained ALMA observations of GRB 190114C beginning 2.2 hr after the burst through program 2018.1.01405.T (PI: T. Laskar) in full linear polarization mode in Band 3, with two 4 GHz-wide basebands centered at 91.5 and 103.5 GHz, respectively. Weather conditions were excellent during the observation. The calibration sources were selected by ALMA, employing J0423-012 as flux density, bandpass, and polarization leakage calibrator, and J0348-274 as complex gain calibrator. The gain calibrator-source cycle time was ≈ 12 minutes, with 10.5 minutes on source, 30 s on the gain calibrator, and the remaining time used for slewing between the two. The scheduling block was repeated three times in succession in order to achieve sufficient parallactic angle coverage to simultaneously derive the instrumental polarization and the Stokes parameters of the leakage calibrator, with parallactic angle coverage on the leakage calibrator spanning $\approx 90^\circ$.

2.3.1. ALMA Data Analysis

We processed the ALMA data using CASA (McMullin et al. 2007), employing standard techniques (Nagai et al. 2016). In

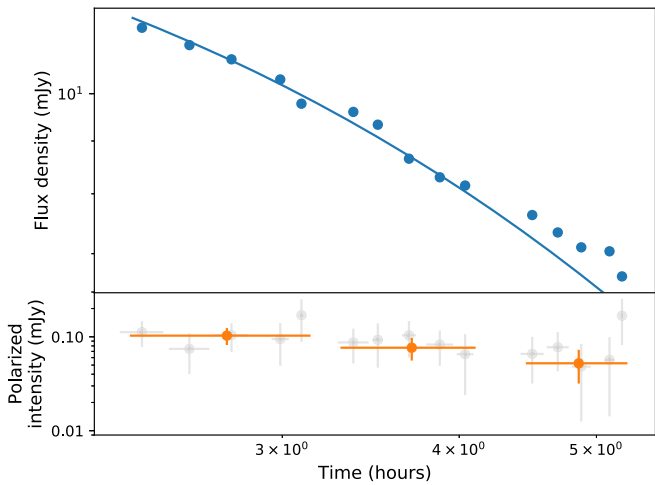


Figure 1. Total intensity (Stokes I) and RS model (top panel; Section 3.2) and linear polarized intensity obtained from a Monte Carlo analysis (gray, and binned orange points, lower panel) for our ALMA observations at 97.5 GHz spanning 2.2–5.2 hr (134–313 minutes) after the burst. The afterglow fades by $\approx 40\%$ during these first three hours of observation, while the polarized intensity drops by $\approx 50\%$.

summary, following bandpass calibration, we computed the complex gain solutions on the polarization calibrator. We used these solutions to estimate the intrinsic Stokes parameters of the polarization calibrator, followed by the cross-hand delays, the XY-phase offset, and the calibrator’s intrinsic polarization. We resolved the phase ambiguities in the Stokes parameters of the calibrator using the estimates derived from the gain calibration, and revised the gain solutions on the polarization calibrator. The ratio of the parallel hand (XX/YY) gains is uniform and within $\approx 2\%$ of unity for all antennas after polarization calibration, while the rms gain ratio is uniform across antennas at the $\approx 1.2\%$ level. The leakage (D-terms) were found to be at the $\approx 1\%$ level for individual antennas, as expected for the ALMA 12 m array (Nagai et al. 2016).

We used flux density values of (4.15 ± 0.08) mJy at 91.5 GHz and (3.89 ± 0.06) mJy at 103.5 GHz for J0423-012 from the ALMA calibrator catalog, to which we fit a power-law model to fix the flux density scale for each channel. We subsequently calibrated the remainder of the data set using standard interferometric techniques (flux density and gain), and generated Stokes $IQUV$ images of the calibrators and the target, as well as an image of the total linear polarization, $P = \sqrt{Q^2 + U^2}$.

The mm-band afterglow is clearly detected in Stokes I , with a signal-to-noise of ≈ 580 , allowing us to divide the source data set into individual scans. We fit for the flux density of the source in the image plane using `imfit`. The derived flux density values are listed in Table 1. The mm afterglow fades by $\approx 40\%$ between 2.2 and 5.2 hr after the burst (Figure 1; top panel).

2.3.2. Measurement of Polarization and Validation Against Potential Instrumental Effects

The P image of GRB 190114C reveals a point source with flux density $61 \pm 14 \mu\text{Jy}$ (unbiased) at a position consistent with the position in the Stokes I image (Figure 2). The rms noise level in the Stokes QUV images is $\approx 10 \mu\text{Jy}$. We split the uv data into the three individual runs of the scheduling block, and re-imaged the target. The detection in the first P image is

6.6σ (statistical), and the polarized intensity declines by $\approx 50\%$ over the course of the observation (Figure 1; bottom panel). The limit on Stokes V is $30 \mu\text{Jy}$, corresponding to a formal 3σ limit on circular polarization of $\Pi_V < 0.3\%$ (statistical only) relative to the mean Stokes I ; however, the 1σ systematic circular polarization calibration uncertainty is $\approx 0.6\%$.

We plot the values of Stokes Q and U , measured by fixing the position and beam parameters using the Stokes I image, in Figure 3. A rotation in the plane of polarization is apparent from the Stokes QU images. As images of P are biased for faint sources, we do not measure P from images of polarized intensity, but rather from the measured QU values directly using a Monte Carlo method. We generate 10^5 random realizations from the individual Q and U measurements and calculate $P = \sqrt{Q^2 + U^2}$, the polarization angle, $\chi = \frac{1}{2} \tan^{-1} \frac{U}{Q}$, and the fractional linear polarization, $\Pi = P/I$. For the latter, we incorporate the uncertainty in the measurement of Stokes I . We plot the derived distributions of P , χ , and Π in Figures 3 and 4, and list the median and standard deviations of the distributions in Table 2.

On applying the polarization calibration to the gain calibrator J0348-274, we find that drift in the linear polarized intensity of the calibrator is $\lesssim 0.15\%$, while its measured polarization angle is stable at the $\lesssim 1\%$ level over the course of the 3 hr observation (Figure 4; bottom panel). Both values are within the specifications of ALMA Cycle 6 polarization observations.

One possible manifestation of any errors arising from leakage calibration is a scattering of flux density in the Stokes QU images away from the phase center. We check this by imaging the gain calibrator, which appears as a point source; observed secondary peaks in both Stokes Q and U images are $\lesssim 0.5\%$ of the peak flux, consistent with noise. We also imaged the upper and lower basebands separately for both the flux density calibrator, phase calibrator, and GRB 190114C. The polarization properties of both calibrators and of GRB 190114C are consistent between the two basebands and thus stable across ALMA Band 3.

As linear polarization observations are a non-standard mode for ALMA, the data were also calibrated and imaged by a data analyst (Erica Keller) at ALMA before delivery. We compared the results of our reduction with those from ALMA, and also by imaging the calibrated measurement set provided by the Observatory. All three sets of images yield results consistent within measurement uncertainty. These tests indicate that the detection of linearly polarization in GRB 190114C is unlikely to arise from a calibration artifact.

3. Basic Considerations

As the focus of this Letter is on the ALMA polarization observations, we defer a discussion of the full multi-wavelength modeling to a future work (T. Laskar et al. 2019, in preparation). To provide context for the polarization detection, here we consider the basic properties of the afterglow at $\lesssim 0.3$ days, during the time of the ALMA observations. We interpret this under the standard synchrotron framework (Sari et al. 1998; Granot & Sari 2002), for a given isotropic equivalent kinetic energy, $E_{K,\text{iso}}$ and circumburst density parameter n_0 (for a constant-density environment) and A_* (for a wind-like environment with density, $\rho \propto R^{-2}$). We assume that the radiation is produced by nonthermal electrons accelerated to a power-law distribution with energy index p ,

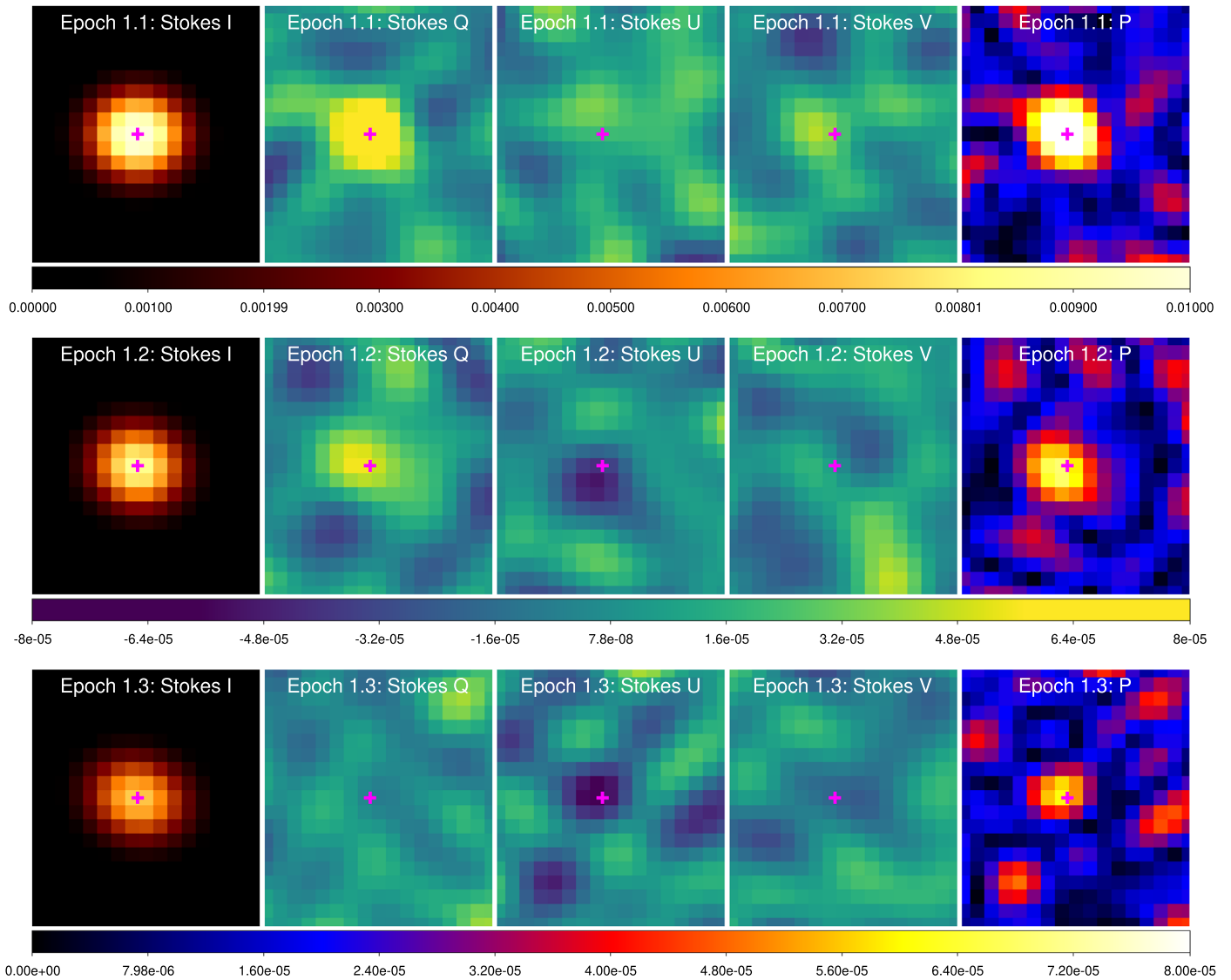


Figure 2. Stokes $IQUV$ and linear polarized intensity, $P = \sqrt{Q^2 + U^2}$ images of the mm-band emission at mean times of 2.74 hr (top), 3.70 hr (center), and 4.86 hr (bottom) after the burst. All images in the same column have the same color bar and scaling parameters. The three color bars from top to bottom provide the scales for the Stokes I , Stokes QUV , and P images, respectively. The images demonstrate the fading Stokes I emission, as well as the rotation of the polarization angle (evolving U/Q ratio).

with a fraction ϵ_e of the post-shock internal energy given to relativistic electrons and a fraction ϵ_B to magnetic fields. In this model, the observed SED is characterized by power laws connected at spectral breaks: the synchrotron self-absorption frequency (ν_a), the characteristic synchrotron frequency (ν_m), and the cooling frequency (ν_c), and is completely specified by the location of these break frequencies and the overall flux density normalization ($F_{\nu,m}$).

3.1. Optical and X-Rays: Circumburst Density Profile

The spectral index¹¹ between the GROND g' - and K -bands, when corrected for Galactic extinction, is $\beta_{\text{NIR-opt}} = -2.4 \pm 0.2$, indicating that extinction is present. The r' -band light curve decays as $\alpha_r = -0.69 \pm 0.02$ between 3×10^{-2} days and 0.3 days, while the X-ray decay rate over this period is $\alpha_X = -1.27 \pm 0.02$, indicating that the optical and X-rays are

on different power-law segments of the synchrotron spectrum. In the slow cooling regime with $\nu_m < \nu_{\text{opt}} < \nu_c < \nu_X$, we expect $\delta\alpha \equiv |\alpha_{\text{opt}} - \alpha_X| = 0.25$, which is inconsistent with the measured $\delta\alpha = 0.58 \pm 0.03$. The only other means for the optical light curve to decay slower than the X-rays is if the system is fast cooling with $\nu_{\text{opt}} < \nu_c < \nu_m < \nu_X$ and the circumburst density profile is a wind-like environment. In this regime, we expect $\alpha_{\text{opt}} \approx -2/3$, which is consistent with the observed r' -band light curve over this period. The shallow optical light curve also places a lower limit on the jet break time, $t_{\text{jet}} \gtrsim 0.3$ days.

The steep X-ray light curve with $\alpha_X \approx -1.3$ in fast cooling implies $\nu_c, \nu_m < \nu_X$, which suggests $p \approx 2.36$. The observed X-ray spectral index over this period is $\beta_X = -0.81 \pm 0.14$. Whereas this is inconsistent with a predicted slope of $\beta_X \approx -1.2$, it is consistent with a spectral slope of $\beta \sim -(p/2 - 1/4) \sim -0.93$ when Klein-Nishina (KN) corrections are taken into account (Nakar et al. 2009). We note that a similar discrepancy in the X-ray spectral index of GRB 161219B was

¹¹ We use the convention $f_\nu \propto \nu^{\alpha\nu\beta}$ throughout.

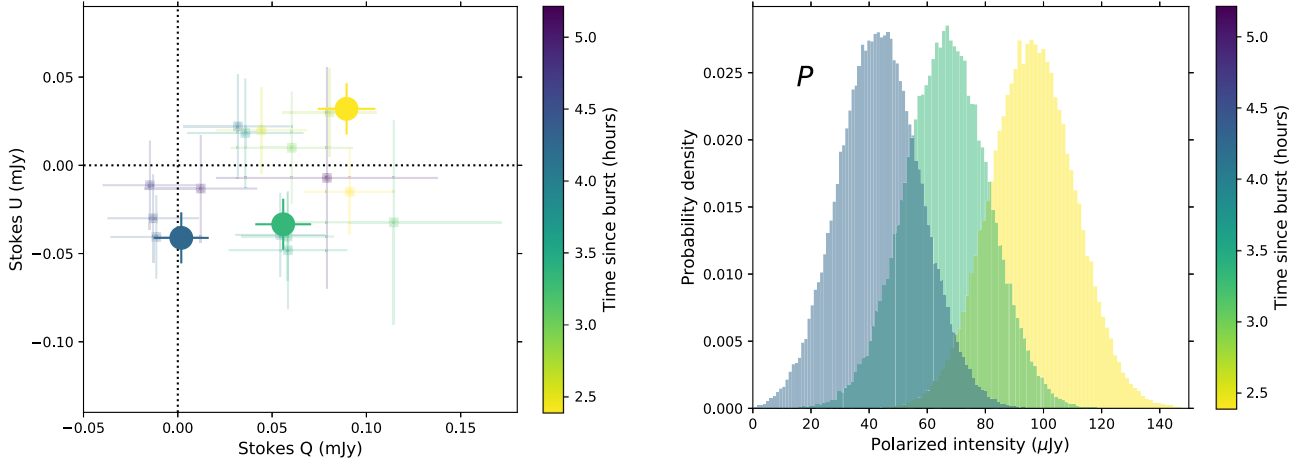


Figure 3. Left panel: Stokes Q vs. Stokes U for our ALMA observations of GRB 190114C at 2.2–5.2 hr after the burst, colored by the time of observation from earliest (yellow) to last (violet). Small squares correspond to individual scans on the target and have large uncertainties, while large circles correspond to measurements from images made with combined uv data from each of the three executions of the scheduling block. The degree of linear polarization is represented by the magnitude of the vector from the origin to the (Q, U) measurement, while the polarization position angle ($\chi = \frac{1}{2} \tan^{-1} \frac{U}{Q}$) is equal to one-half of the angle subtended by that vector and the x -axis. The plot has the same linear scale on both axes, with the origin displaced. Right panel: probability density for the total polarized intensity at mean times of 2.74 hr (yellow), 3.70 hr (green), and 4.86 hr (blue) after the burst, generated by sampling from the distributions of the individual measured Stokes Q and U values for these three epochs, and assuming Gaussian errors. The polarized intensity decreases with time.

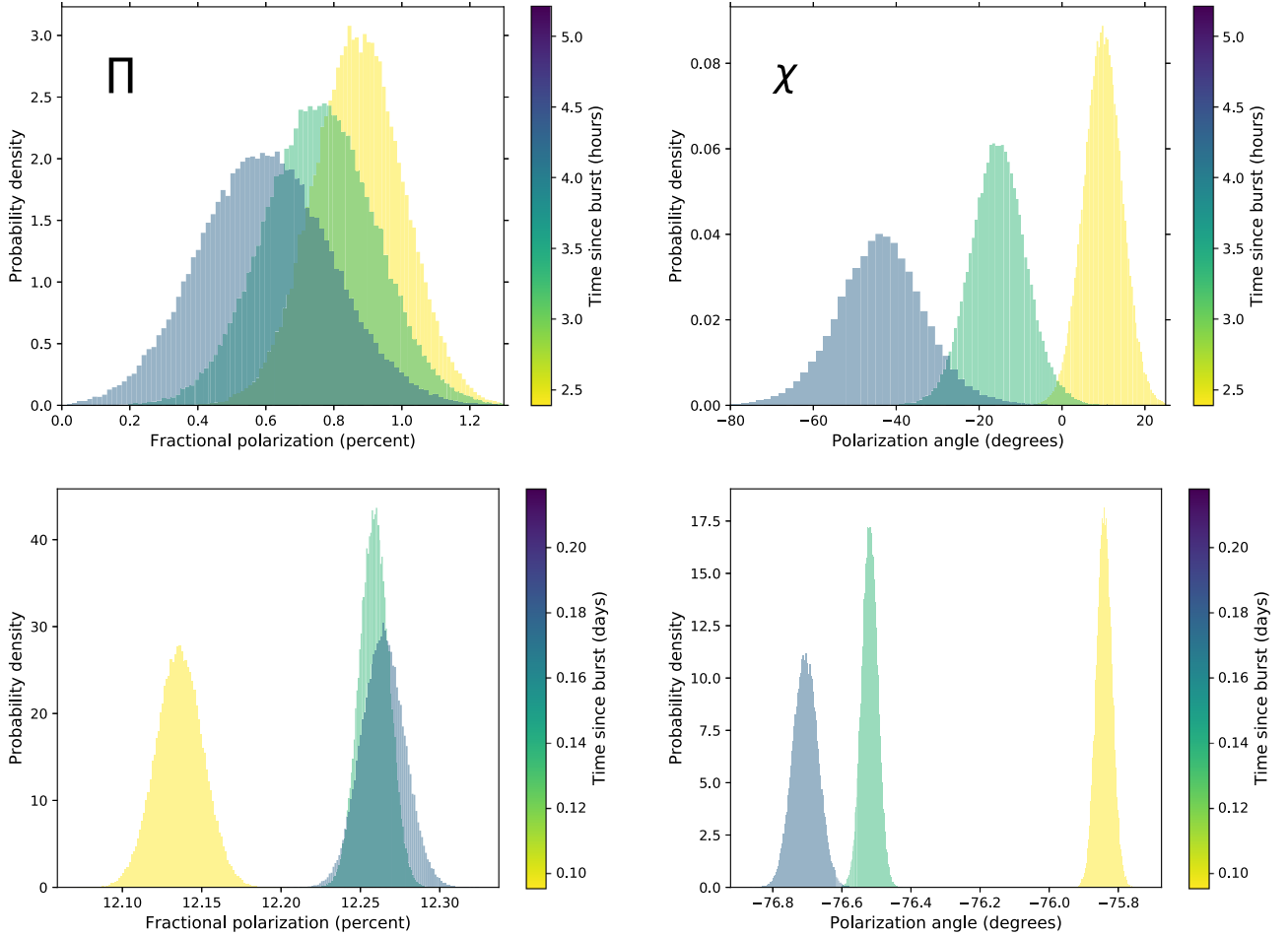


Figure 4. Top row: probability density for the fractional linear polarization ($\Pi = P/I$, left panel) and polarization angle (χ , right panel) at mean times of 2.74 hr (yellow), 3.70 hr (green), and 4.86 hr (blue) after the burst, generated by sampling from the probability density of the total polarized intensity (Figure 3) and the total intensity in these three epochs (assuming Gaussian errors for the latter). The fractional polarization decreases with time, while the polarization angle rotates by $\delta\chi = 54 \pm 13$ degrees. Bottom row: same as top row but for the complex gain calibrator, which was not used in the polarization calibration. The fractional polarization is stable at $\lesssim 0.15\%$ and the polarization angle within $\lesssim 1^\circ$, conforming to the specifications for linear polarization observations in ALMA Cycle 6.

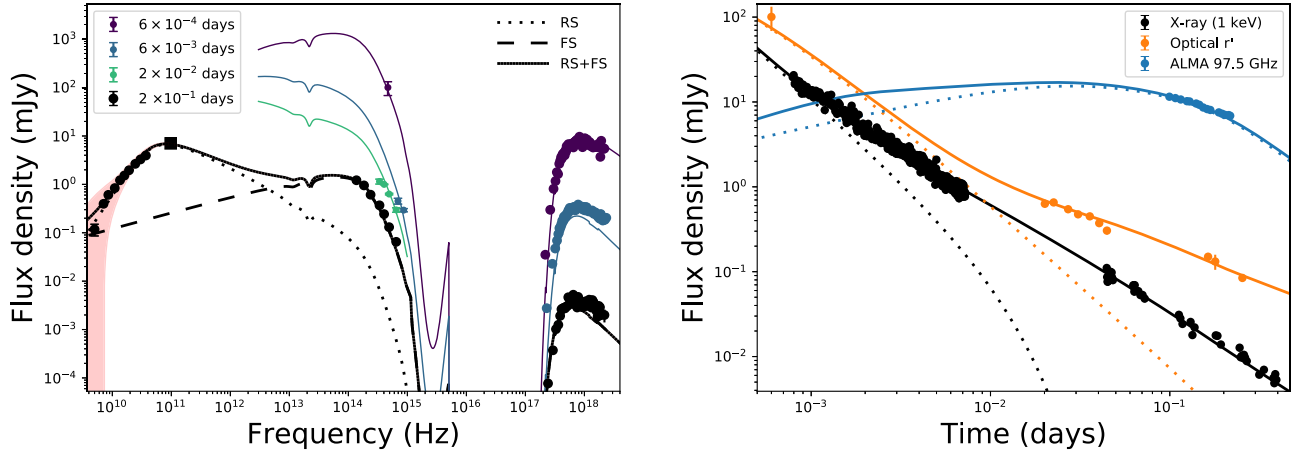


Figure 5. Left panel: SEDs at 6×10^{-4} days (MASTER; Tyurina et al. 2019), 6×10^{-3} days (*Swift*/UVOT), 2×10^{-2} days (NOT; Selsing et al. 2019) and 0.2 days (VLA, ALMA, and GROND; Bolmer & Schady 2019) after the burst, with an afterglow model (lines) decomposed at 0.2 days into forward shock (dashed) and reverse shock (dotted) components. The RS model employs $\nu_{a,r} \approx 40$ GHz, $\nu_{m,r} \approx 70$ GHz, $\nu_{c,r} \approx 4 \times 10^{15}$ Hz, and $F_{\nu,m,r} \approx 14$ mJy at 0.2 days. The red shaded region indicates the expected variability due to scintillation in the radio. The model explains the radio to X-ray SED, the X-ray light curve, and the optical light curve before 0.2 days. The Compton $Y \approx 20$ for this model is high, and the discrepancy in the X-rays above $\approx 10^{18}$ Hz may arise from the KN correction. Right panel: X-ray (1 keV), optical $r'/R/Rc$ -band, and ALMA 97.5 GHz light curves of GRB 190114C from the first MASTER detection at $\approx 6 \times 10^{-4}$ days to ≈ 0.3 days, together with the same afterglow model as the left panel, with the RS contribution indicated (dotted lines).

Table 2
ALMA Band 3 (97.5 GHz) Polarization Measurements of GRB 190114C

Time (days)	Q (μ Jy)	σ_Q (μ Jy)	U (μ Jy)	σ_U (μ Jy)	P (μ Jy)	σ_P (μ Jy)	χ (deg)	σ_χ (deg)	Π (%)	σ_Π (%)
0.114	89.5	14.6	32.0	15.3	96.3	14.6	9.8	4.6	0.87	0.13
0.154	55.9	14.5	-33.4	14.8	66.7	14.4	-15.4	6.6	0.76	0.16
0.202	1.84	14.5	-41.1	14.6	43.7	14.0	-43.7	11.7	0.60	0.19

also attributable to KN corrections (Laskar et al. 2018a). We leave a detailed exploration of KN corrections to further work. In summary, the optical and X-ray light curves until 0.3 days are consistent with FS emission in wind-like environment with $p \approx 2.36$ and $t_{\text{jet}} \gtrsim 0.3$ days.

3.2. Radio and Millimeter: RS

The radio SED at 0.2 days comprising the VLA cm-band and ALMA mm-band data (Figure 5) can be fit with a broken power-law model, transitioning from $\beta = 2$ (fixed) to $\beta = 0.3 \pm 0.2$ at $\nu_{\text{break}} = 24 \pm 4$ GHz. In addition, the mean Stokes I intra-band spectral index between the two ALMA basebands at 91.5 and 103.5 GHz is ≈ -0.4 , implying that the mm-band emission is optically thin at this time. The optical to mm-band spectral index of $\beta_{\text{mm-opt}} = -0.24 \pm 0.01$ between the GROND K -band observation and the ALMA detection at 0.16 days is inconsistent with a single power-law extrapolation from the optical.¹² This shallow slope cannot be caused by the location of $\nu_{m,f}$ between the radio and optical bands¹³ because all light curves at $\nu_{a,f} < \nu < \nu_{m,f}$ should be flat in the wind model (or rising in the interstellar medium (ISM) model), while the ALMA light curve is declining over this period. Thus, the radio and mm-band emission arises from a separate component than that responsible for the X-ray and optical emission. We

note that a similar radio-to-X-ray spectral index of $\beta_{\text{radio,opt}} \approx -0.25$ in the case of GRB 130427A indicated the presence of an RS in that system (Laskar et al. 2013). The early optical r' -band light curve declines as $\alpha_{\text{opt}} = -1.4 \pm 0.1$ between the MASTER observation at $\approx 6 \times 10^{-4}$ days¹⁴ and the NOT observation at $\approx 2 \times 10^{-2}$ days, flattening to $\alpha = -0.69 \pm 0.02$ between the NOT observation and the GROND observation at 0.16 days (Figure 5). The steep optical light curve at $\lesssim 2 \times 10^{-2}$ days can also not be explained as FS emission.

We find that propagating the excess emission component dominating the radio and mm-band data at ≈ 0.2 days earlier, using the RS light curve evolution from Zou et al. (2005) and the SED shape from Laskar et al. (2013), can explain the optical observations at < 0.2 days, provided $F_{\nu,m} \propto t^{-0.9}$ and $\nu_m \propto t^{-1.4}$ for this component (Figure 5). This matches a Newtonian RS with¹⁵ $g \sim 3$, which is higher than expected for the wind environment but not unprecedented (Laskar et al. 2013, 2016, 2018a; Perley et al. 2014). The parameters for the FS that match the X-ray and optical light curves at $\lesssim 0.3$ days are $p \approx 2.36$, $\epsilon_e \approx 0.9$, $\epsilon_B \approx 6 \times 10^{-3}$, $A_* \approx 1.5 \times 10^{-2}$, $E_{\text{K,iso}} \approx 7 \times 10^{52}$ erg, and $A_V \approx 2.2$ mag. For these parameters, the FS is fast cooling until ≈ 0.2 days, with the spectral ordering $\nu_{a,f} < \nu_{\text{radio}} < \nu_{c,f} \approx \nu_{\text{opt}} < \nu_{m,f} < \nu_X$ for the FS at 10^{-2} days. However, we note that we do not locate $\nu_{a,f}$ and thus the model parameters are subject to some degeneracies (possibly explaining the high value of ϵ_e). We defer a more

¹² We note that extinction correction at optical K -band is expected to be modest. Explaining the declining mm-near-infrared (NIR) SED as due to extinguished FS emission would require $A_K \approx 4.5$ mag (or $A_V \approx 35$ mag for a Small Magellanic Cloud extinction curve), which would completely extinguish the ultraviolet (UV)/optical emission.

¹³ The subscript ‘‘f’’ refers to the FS.

¹⁴ While the MASTER observation is calibrated to R -band, the difference between r' - and R -bands is negligible for this argument.

¹⁵ The Lorentz factor of the RS ejecta, $\Gamma_{\text{ej}} \propto R^{-g}$.

complete analysis of the FS and the joint RS–FS dynamics to future work.

4. Discussion

We now derive constraints on the magnetic field structure in the jet using our polarization measurement. The low level of measured linear polarization in the mm-band,¹⁶ $\Pi \sim 0.6\text{--}0.9\%$, rules out an ordered transverse magnetic field (B_{ord}) in the ejecta with an angular coherence length $\theta_B \gtrsim 1/\Gamma$, where Γ is the Lorentz factor of the emitting region, as such a field would produce a polarization of several tens of percent (Granot 2003; Granot & Königl 2003; Lyutikov et al. 2003). We now consider scenarios where the received radiation is a superposition of distinct emission components in regions comprising a transverse ordered field (B_{ord}) on the one hand, and a random (B_{rand}) magnetic field (Granot & Königl 2003) on the other. Such a scenario might correspond to co-located field components such as a shocked ISM with an ordered upstream field compressed at the FS and a random shock-generated B_{rand} , or to the superposition of emission from two distinct regions, e.g., a dominant B_{ord} in the shocked ejecta and a dominant B_{rand} in the shocked ISM. In such scenarios, Π and χ depend on the ratio of the intensities of synchrotron radiation due to the two magnetic field components, $I_{\text{ord}}/I_{\text{rand}} \approx \langle B_{\text{ord}}^2/B_{\text{rand}}^2 \rangle$, and thus can vary with time (Granot & Königl 2003). However, the significant change in χ we measure would require comparable polarized intensities from the two components, with a ratio varying on the dynamical time. This is not easy to realize at $\ll t_{\text{jet}}$, and where the 97.5 GHz light curve is dominated by RS emission, and thus such scenarios are disfavored.

Next, we consider a model where the observed polarization is the sum of emission from intrinsically polarized but mutually incoherent patches, each with a magnetic field ordered over a typical angular scale, θ_B (Granot & Königl 2003; Nakar & Oren 2004; Granot & Taylor 2005). In this model the visible region, $\theta \sim 1/\Gamma_{\text{ej}}$, around the line of sight gradually increases as the jet decelerates. The number of patches contributing to the observed emission is given by $N \sim (\Gamma_{\text{ej}}\theta_B)^{-2}$. In general, the ejecta lags behind the FS and $\Gamma_{\text{ej}} \lesssim \Gamma_{\text{sh}}$; however, a Newtonian RS does not significantly decelerate the ejecta (Kobayashi 2000). For $g \approx 3$ and $k = 2$, we have $\Gamma_{\text{ej}}/\Gamma_{\text{sh}} \propto (t/t_{\text{dec}})^{-[g-(3-k)/2]/[(4-k)(2g+1)]} \propto (t/t_{\text{dec}})^{-5/28}$ (Granot & Taylor 2005). Taking $t_{\text{dec}} \approx T_{90} = 116$ s from *Fermi*/GBM¹⁷, $\Gamma_{\text{ej}}/\Gamma_{\text{sh}} \approx 0.5$ at the time of our mm-band polarization measurement. At this time, the Lorentz factor of the fluid shocked by the FS, $\Gamma_{\text{sh}} = 3.7 \left[\frac{E_{\text{K,iso},52}(1+z)}{A_* t_{\text{days}}} \right]^{1/4} \approx 30$ (Granot & Sari 2002), so that $\Gamma_{\text{ej}} \approx 15$.

The maximum degree of polarization, $\Pi_0 = (1-\beta)/(5/3-\beta)$, where β is the spectral index (Granot & Taylor 2005). Because the ALMA band is near the peak of the SED (Figure 5), we take $\beta \sim 0$, yielding $\Pi_0 \sim 0.6$. The observed polarization is a random walk of N steps in the QU plane, with $\Pi \sim \Pi_0/\sqrt{N} \sim \Pi_0\Gamma_{\text{ej}}\theta_B$, which implies $\theta_B \sim \Pi/(\Gamma_{\text{ej}}\Pi_0) \approx 10^{-3}$. The uncertainty on this

¹⁶ The observed low degree of linear polarization is unlikely to result from Faraday depolarization, as the latter is strongly suppressed at these frequencies (Granot & Taylor 2005). Furthermore, we find no evidence of increased polarization upon decreasing our observing bandwidth by splitting the data into the two basebands (Section 2.3.2).

¹⁷ The UVOT light curve is definitely declining by $t_{\text{dec}} = 566$ s (Siegel & Gropp 2019). Taking t_{dec} equal to this upper limit only increases Γ_{ej} by $\approx 30\%$.

estimate from the signal-to-noise of the measurement of Π is $\approx 15\%$; however, larger systematic uncertainties arise from the approximations used in the RS dynamics as well as the stochastic nature of the 2D random walk.

In this model, the polarization angle is expected to vary randomly over the dynamical timescale as new patches enter the visible region. The mm-band light curve spans a factor of ≈ 2.2 in time. During this period, Γ_{sh} declines from ≈ 34 to ≈ 28 from our afterglow model and Γ_{ej} declines from ≈ 16 to ≈ 11 . Assuming θ_B remains constant, the number of emitting patches increases by a factor of ≈ 2 over this period, which may be sufficient to change the average χ as we observe. Whereas we expect fluctuations in Π over this period, our measurements do not have sufficient signal-to-noise to resolve such variations (Figure 3).

Finally, we note that the gradual change observed in χ rules out any globally axisymmetric magnetic field configuration, regardless of our viewing angle and of the jet’s exact axisymmetric angular structure; for example: (i) a global toroidal magnetic field (Lazzati et al. 2004; Granot & Taylor 2005); and (ii) an axisymmetric jet viewed from an angle $\theta_{\text{obs}} > 0$ from its symmetry axis together with a shock-produced random magnetic field B_{rand} that is symmetric around the local shock normal (tangled in three dimensions on angular scales $\ll 1/\Gamma$, with some non-negligible degree of anisotropy, as a locally isotropic field would produce no net polarization), as in this case the direction of polarization is expected to remain constant well before the jet break time t_{jet} (Ghisellini & Lazzati 1999; Sari 1999; Granot & Königl 2003).














5. Conclusions

We present the first detection and measurement of the temporal evolution of linearly polarized emission in the radio/millimeter afterglow of a GRB, and validate that our measurement does not arise from a calibration artifact. Our detection constitutes the first measurement of a polarized RS signature at radio or millimeter frequencies. The degree of linear polarization decreases from $\Pi = (0.87 \pm 0.13)\%$ to $\Pi = (0.60 \pm 0.19)\%$ from 2.2 to 5.2 hr after the burst, and the polarization position angle rotates from $\chi = (10 \pm 5)^\circ$ to $\chi = (-44 \pm 12)^\circ$ over this period. The smooth variation in χ rules out axisymmetric models such as a global toroidal field in the GRB jet. If the emission arises from small patches of coherent magnetization, then the size of these regions is constrained to $\theta_B \approx 10^{-3}$ radian. Future work on GRB 190114C that evaluates the degeneracies in the FS parameters and compares the derived properties of the forward and reverse shocks to infer the dynamics of the jet, may refine these parameters. ALMA polarimetric observations of a sample of GRBs will reveal whether sub-percent levels of polarization are ubiquitous, thus constraining global jet models.

We thank Mark Lacy and Robert Laing for helpful discussions, Erica Keller at ALMA for providing the calibrated measurement sets for a verification of the science results, and the anonymous referee for feedback. This Letter makes use of the following ALMA data: ADS/JAO.ALMA#2018.1.01405.T. ALMA is a partnership of ESO (representing its member states), NSF (USA) and NINS (Japan), together with NRC (Canada), NSC and ASIAA (Taiwan), and KASI (Republic of Korea), in cooperation with the Republic of Chile. The Joint ALMA Observatory is operated by ESO, AUI/NRAO and NAOJ. VLA observations for this study were obtained via project 18A-088.

The National Radio Astronomy Observatory is a facility of the National Science Foundation operated under cooperative agreement by Associated Universities, Inc. K.D.A. acknowledges support provided by NASA through the NASA Hubble Fellowship grant #HST-HF2-51403.001 awarded by the Space Telescope Science Institute, which is operated by the Association of Universities for Research in Astronomy, Inc., for NASA, under contract NAS5-26555. J.G. and R.G. are supported by the Israeli Science Foundation under grant No. 719/14. The Berger Time-Domain Group at Harvard is supported in part by NSF under grant AST-1714498 and by NASA under grant NNX15AE50G. R.B.D. acknowledges support from the National Science Foundation under grant 1816694. This work makes use of data supplied by the UK Swift Science Data Centre at the University of Leicester and of data obtained through the High Energy Astrophysics Science Archive Research Center On-line Service, provided by the NASA/Goddard Space Flight Center.

ORCID iDs

Tanmoy Laskar  <https://orcid.org/0000-0003-1792-2338>
 Kate D. Alexander  <https://orcid.org/0000-0002-8297-2473>
 Ramandeep Gill  <https://orcid.org/0000-0003-0516-2968>
 Jonathan Granot  <https://orcid.org/0000-0001-8530-8941>
 Edo Berger  <https://orcid.org/0000-0002-9392-9681>
 C. G. Mundell  <https://orcid.org/0000-0003-2809-8743>
 J. Bolmer  <https://orcid.org/0000-0002-3373-0646>
 Paul Duffell  <https://orcid.org/0000-0001-7626-9629>
 Hendrik van Eerten  <https://orcid.org/0000-0002-8680-8718>
 Wen-fai Fong  <https://orcid.org/0000-0002-7374-935X>
 Shiho Kobayashi  <https://orcid.org/0000-0001-7946-4200>
 Raffaella Margutti  <https://orcid.org/0000-0003-4768-7586>
 Patricia Schady  <https://orcid.org/0000-0002-1214-770X>

References

Akerlof, C., Balsano, R., Barthelmy, S., et al. 1999, *Natur*, 398, 400
 Alexander, K. D., Laskar, T., Berger, E., et al. 2017, *ApJ*, 848, 69
 Barthelmy, S. D., Barbier, L. M., Cummings, J. R., et al. 2005, *SSRv*, 120, 143

Bolmer, J., & Schady, P. 2019, *GCN*, 23702, 1
 Burrows, D. N., Hill, J. E., Nousek, J. A., et al. 2005, *SSRv*, 120, 165
 Frederiks, D., Golenetskii, S., Aptekar, R., et al. 2019, *GCN*, 23737, 1
 Gehrels, N., Chincarini, G., Giommi, P., et al. 2004, *ApJ*, 611, 1005
 Ghisellini, G., & Lazzati, D. 1999, *MNRAS*, 309, L7
 Granot, J. 2003, *ApJL*, 596, L17
 Granot, J., & Königl, A. 2003, *ApJL*, 594, L83
 Granot, J., & Sari, R. 2002, *ApJ*, 568, 820
 Granot, J., & Taylor, G. B. 2005, *ApJ*, 625, 263
 Gropp, J. D., Kennea, J. A., Klingler, N. J., et al. 2019, *GCN*, 23688, 1
 Gruzinov, A., & Waxman, E. 1999, *ApJ*, 511, 852
 Hamburg, R., Veres, P., Meegan, C., et al. 2019, *GCN*, 23707, 1
 Kann, D. A., Thoene, C. C., Selsing, J., et al. 2019, *GCN*, 23710, 1
 Kobayashi, S. 2000, *ApJ*, 545, 807
 Kocevski, D., Omodei, N., Axelsson, M., et al. 2019, *GCN*, 23709, 1
 Laskar, T., Alexander, K. D., Berger, E., et al. 2016, *ApJ*, 833, 88
 Laskar, T., Alexander, K. D., Berger, E., et al. 2018a, *ApJ*, 862, 94
 Laskar, T., Berger, E., Margutti, R., et al. 2018b, *ApJ*, 859, 134
 Laskar, T., Berger, E., Zauderer, B. A., et al. 2013, *ApJ*, 776, 119
 Lazzati, D., Covino, S., Gorosabel, J., et al. 2004, *A&A*, 422, 121
 Lyutikov, M., Pariev, V. I., & Blandford, R. D. 2003, *ApJ*, 597, 998
 McMullin, J. P., Waters, B., Schiebel, D., Young, W., & Golap, K. 2007, in ASP Conf. Ser. 376, *Astronomical Data Analysis Software and Systems XVI*, ed. R. A. Shaw, F. Hill, & D. J. Bell (San Francisco, CA: ASP), 127
 Meegan, C., Lichti, G., Bhat, P. N., et al. 2009, *ApJ*, 702, 791
 Mirzoyan, R., Noda, K., Moretti, E., et al. 2019, *GCN*, 23701, 1
 Mundell, C. G., Kopač, D., Arnold, D. M., et al. 2013, *Natur*, 504, 119
 Nagai, H., Nakanishi, K., Paladino, R., et al. 2016, *ApJ*, 824, 132
 Nakar, E., Ando, S., & Sari, R. 2009, *ApJ*, 703, 675
 Nakar, E., & Oren, Y. 2004, *ApJL*, 602, L97
 Perley, D. A., Cenko, S. B., Corsi, A., et al. 2014, *ApJ*, 781, 37
 Poole, T. S., Breeveld, A. A., Page, M. J., et al. 2008, *MNRAS*, 383, 627
 Roming, P. W. A., Kennedy, T. E., Mason, K. O., et al. 2005, *SSRv*, 120, 95
 Sari, R. 1999, *ApJL*, 524, L43
 Sari, R., & Piran, T. 1999, *ApJL*, 517, L109
 Sari, R., Piran, T., & Narayan, R. 1998, *ApJL*, 497, L17
 Selsing, J., Fynbo, J. P. U., Heintz, K. E., & Watson, D. 2019, *GCN*, 23695, 1
 Siegel, M. H., & Gropp, J. D. 2019, *GCN*, 23725, 1
 Toma, K., Ioka, K., & Nakamura, T. 2008, *ApJL*, 673, L123
 Tyurina, N., Lipunov, V., Kuznetsov, A., et al. 2019, *GCN*, 23690, 1
 van der Horst, A. J., Paragi, Z., de Bruyn, A. G., et al. 2014, *MNRAS*, 444, 3151
 Williams, P. K. G., Clavel, M., Newton, E., & Ryzhkov, D. 2017, Pwkit: Astronomical Utilities in Python, Astrophysics Source Code Library, ascl:1704.001
 Zhang, B., & Kobayashi, S. 2005, *ApJ*, 628, 315
 Zou, Y. C., Wu, X. F., & Dai, Z. G. 2005, *MNRAS*, 363, 93